Boundary-Layer Meteorol (2011) 138:299–319
DOI 10.1007/s10546-010-9555-3

ARTICLE

Influences of Tidal Fronts on Coastal Winds Over an Inland Sea

Rui Shi · Xinyu Guo · Hidetaka Takeoka

Received: 16 January 2010 / Accepted: 19 October 2010 / Published online: 6 November 2010

Abstract A regional numerical model of the atmosphere was applied to an inland sea, the Seto Inland Sea in Japan, to study the influence of sea-surface temperature (SST) variations, accompanied by a tidal front, on the coastal winds in summer when tidal fronts fully develop. After confirmation of the model performance, two sensitivity simulations, which used spatially uniform SST with the highest and lowest values over the study area, were performed. The control and sensitivity simulations show that the mean wind speeds were apparently reduced by the low SST and the SST gradient accompanying the tidal front. The comparison of the terms in the momentum equations in control and sensitivity simulations indicates that the change of the perturbation pressure gradient force with the SST gradient is the most important factor in the modification of near-surface winds with SST variations. When the air flows across a tidal front, the air cools over the low SST area and warms over the high SST area. Consequently, the surface perturbation pressure increases over the low SST area and decreases over the high SST area. This adjustment in surface perturbation pressure produces an additional pressure gradient force with direction from the low SST area to the high SST area that decelerates the surface wind in the area upwind of the tidal front and accelerates the surface wind downwind of the tidal front.

Keywords Coastal winds · Numerical simulation · Sea-surface temperature · Seto Inland Sea · Tidal fronts

R. Shi
Graduate School of Science and Engineering, Ehime University, Bunkyo-cho 2-5, Matsuyama 790-8577, Japan

X. Guo (✉) · H. Takeoka
Center for Marine Environmental Studies, Ehime University, Bunkyo-cho 2-5, Matsuyama 790-8577, Japan
e-mail: guoxinyu@sci.ehime-u.ac.jp

1 Introduction

The influences of sea-surface temperature (SST) fronts on atmospheric processes have been reported in many regions such as the eastern Pacific equatorial area (e.g. Lindzen and Nigam 1987; Wallace et al. 1989), the Gulf Stream (Mahrt et al. 2004; Song et al. 2006; Minobe et al. 2008), and the Kuroshio and the Kuroshio extension (Nonaka and Xie 2003). These observation- or simulation-based studies indicate a positive correlation between surface winds and the SST (Xie 2004; Chelton et al. 2001, 2004; Chelton 2005). In addition, wind convergence, humidity, wind stress curl and the structure of the marine atmospheric boundary layer are also affected by SST fronts (Small et al. 2008).

According to Yanagi and Koike (1987), oceanic fronts can be classified into three types: coastal water fronts, shelf fronts and open ocean fronts. Compared to continental shelf and open ocean fronts, the modification of the surface wind by the coastal water front has been less studied. There are four major types of coastal water fronts (Yanagi and Koike 1987): an estuarine front located near a river mouth and essentially a salinity front; a thermal effluent front close to a power plant for which scale and location are limited; a thermohaline front formed in winter in a transition zone between cold coastal water and warm oceanic water outside a bay or an inland sea; and a tidal front formed in summer in a transition zone between vertical well-mixed water and stratified water inside a bay or an inland sea. Amongst these types, the tidal front has the highest potential to affect the winds inside a bay or an inland sea, due both to its location of formation and its formation season.

Two hypotheses have been proposed to explain the mechanism of the surface wind response to oceanic SST fronts. With an application of a one-dimensional planetary boundary-layer model to the response of the surface winds to tropical instability waves in the eastern equatorial Pacific, Lindzen and Nigam (1987) found that the horizontal structure in the marine atmospheric boundary-layer wind field is mainly driven by horizontal pressure gradients developing in response to the boundary-layer baroclinicity induced by the underlying SST gradient. Song et al. (2006) suggested that the perturbation pressure gradient resulting from thermal forcing with SST fronts accounts for the decrease in wind speed when air moves from warm water to cold water in the Gulf Stream region and for the increase in wind speed when air moves from cold water to warm water. They also found that the adjustment of the surface wind in response to the front occurred as a result of vertical motions induced by the horizontal convergence/divergence, while advection and Coriolis forces are additional factors.

Wallace et al. (1989) and Hayes et al. (1989) presented an alternative hypothesis. From the fact that surface winds are strongest over warm water to the north of the strongest SST gradients in the eastern equatorial Pacific, they argued that the vertical momentum transport by convective mixing, which brings fast moving upper layer air down to the surface layer, is the dominant process in the intensification in surface winds over warm water. Recently, Skyllingstad et al. (2007) applied a two-dimensional large-eddy simulation model to study the mean wind response to an SST front, and found that the turbulent momentum flux divergence dominates the velocity field tendency while the pressure forcing accounts for relative small changes to the momentum flux. Therefore, the debate over the mechanism has not been resolved yet (Small et al. 2008).

The Seto Inland Sea is a semi-enclosed coastal sea surrounded by the Honshu, Shikoku and Kyushu Islands of Japan (Fig. 1b). Its coastline is complex due to the presence of many peninsulas and islands, which divides the sea into wide basins and narrow channels (Takeoka 2002). The difference in vertical mixing ability caused by the strong tidal currents in the channels and the weak tidal currents in the wide basins induces the formation of tidal fronts

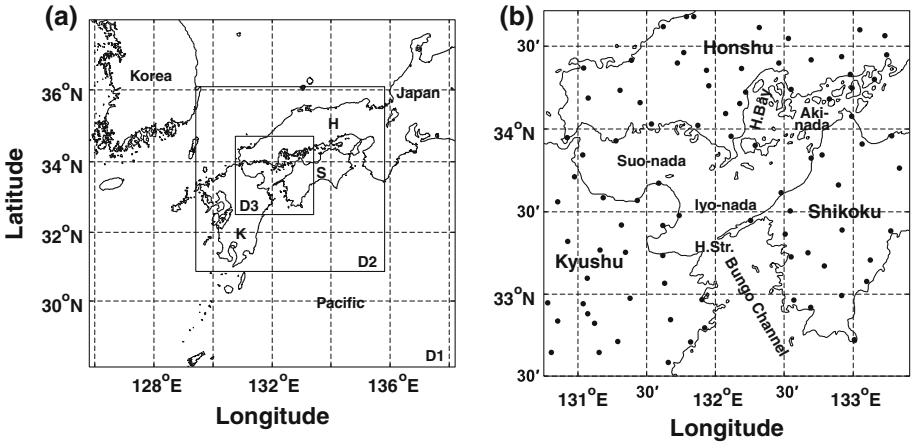

Fig. 1 Map of model domains (**a**). *D1*, *D2* and *D3* denote three model domains in Seto-MM5. The Seto Inland Sea is surrounded by Honshu (H), Shikoku (S) and Kyushu (K) Islands. Detailed map of D3 domain (**b**), in which *H. Str.* denotes the Hayasui Strait, *H. Bay* denotes the Hiroshima Bay, and *black dots* denote the AMeDAS observatories

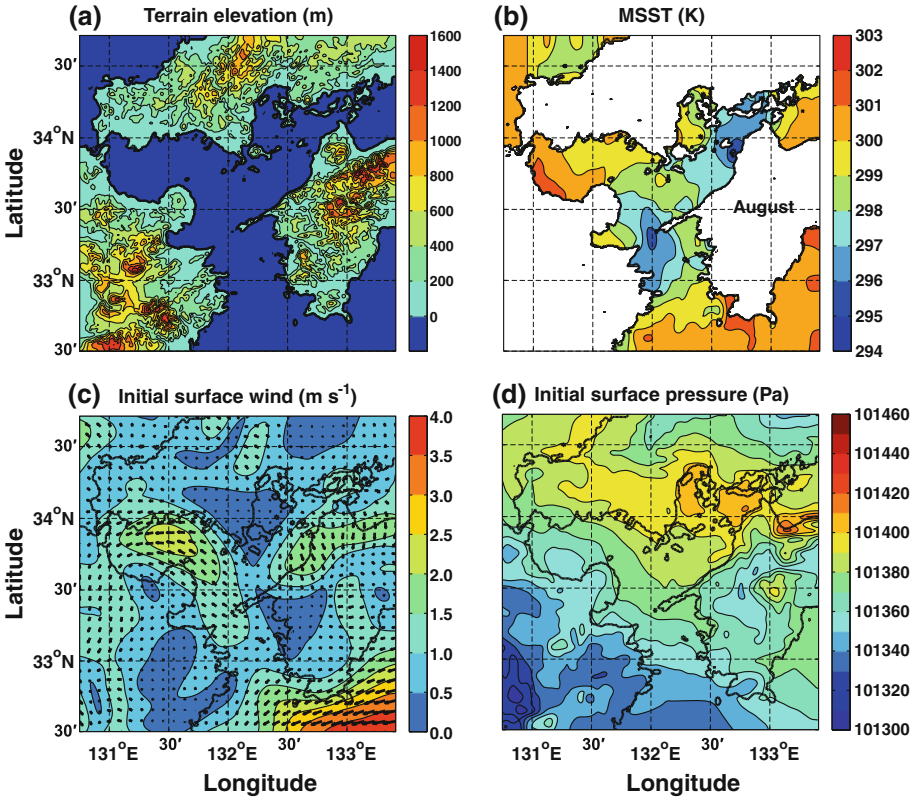

Fig. 2 Topography of D3 domain (**a**). The mean SST in August from 1964 to 1993 in the D3 domain (**b**) used in the control simulation of Seto-MM5. Initial conditions for surface winds and surface pressures are shown in (**c**) and (**d**)

around the narrow channels in summer (Yanagi and Okada 1993). The SST around tidal fronts is lower inside the channel than outside it (Fig. 2b), and this apparent SST gradient can be observed from May to September in the Seto Inland Sea (Yanagi and Koike 1987). The presence of tidal fronts in summer is a common feature in many island seas and bays (Simpson and Hunter 1974).

In addition to seasonally mean winds, the diurnal wind variation is an important feature of the coastal wind. The sea/land breeze is a representative diurnal wind system in inland seas. The difference in the heating capacity of land and the adjacent water mass is the essential cause of the development of the sea/land breeze. Diurnal variations in ground temperature, static stability, Coriolis force, prevailing wind, and topography including the size and shape of land and coastline also affect the development of sea/land breeze (Simpson 1994). Mizuma (1995, 1998) has described the sea/land-breeze system in the Seto Inland Sea, but did not pay attention to either the spatial structure of the sea/land breeze offshore or the influence of the SST front on the sea/land-breeze system in the Seto Inland Sea.

According to the studies on the influence of SST fronts on the wind fields over the open ocean (Small et al. 2008), we expect that tidal fronts affect the coastal winds to some extent. In addition to the influences of tidal fronts on seasonally mean winds and the diurnal cycle, we need also to understand the mechanism responsible for the response of coastal winds to tidal fronts, since the spatial scale of tidal fronts is different from SST fronts in the open oceans. For these purposes, a regional atmospheric model was used firstly to reproduce a typical summer wind field in the western Seto Inland Sea and then to examine the influence of tidal fronts on coastal winds.

The model configuration and necessary data are described in Sect. 2. In Sect. 3.1, the model results are compared with observations; in Sect. 3.2, the horizontal distribution of mean wind and diurnal wind variations along the coast of the western Seto Inland Sea are presented. In order to examine the influence of SST gradient on the mean wind and diurnal wind variations, two sensitivity experiments with spatially uniform low and high SSTs were carried out. The comparison of the two sensitivity experiments with the control simulation is given in Sect. 3.3. Changes in the terms of the momentum equations with SST are presented in Sect. 4 and a summary is given in Sect. 5.

2 Model Configuration and Data

In this study, the fifth-generation Pennsylvania State University–National Center for Atmospheric Research Mesoscale Model (MM5) was applied to an inland sea, the Seto Inland Sea in Japan, to examine the response of coastal winds in summer to tidal fronts. MM5 has been used extensively to simulate the atmospheric processes over the ocean (e.g. Song et al. 2004, 2006; Chen et al. 2005). The model for the Seto Inland Sea (hereafter called Seto-MM5) includes three nested domains: D1, D2 and D3, with a horizontal resolution of 9, 3 and 1 km respectively (Fig. 1a). The outermost domain (D1) covers western Japan; the middle domain (D2) covers the entire Seto Inland Sea, and the innermost domain (D3) focuses on the western Seto Inland Sea (Fig. 1b) where the tidal front is apparent (Fig. 2b). Two-way nesting was used so that the interactions between domains are considered.

The model topography was produced from the United States Geological Survey (USGS) data; the resolution of the original USGS data was 9 min for D1, 2 min for D2, and 30 s, i.e., the standard global 30 arc second elevation data, for D3. The land use and vegetation data were also obtained from the USGS global land cover characteristics database with 24 vegetation categories (Grell et al. 1994).

The medium range forecast planetary boundary-layer scheme in MM5 was chosen in our simulations since it is an efficient scheme based on the Troen–Mahrt non-local vertical diffusion theory (Troen and Mahrt 1986), and has been demonstrated to successfully simulate realistic daytime boundary-layer structure (Hong and Pan 1996). The surface roughness length over the water is calculated using Charnock's equation $z_0 = Cu_*^2/g + o$, where C is the Charnock coefficient ($= 0.032$), u_* is the friction velocity ($\mathrm{m\,s^{-1}}$), g is the acceleration due to gravity ($= 9.806\,\mathrm{m\,s^{-2}}$), and o is a small constant ($= 10^{-4}$).

Following Lo et al. (2007), who presented the benefit of using the Noah land-surface model (Chen and Dudhia 2001) in simulating the sea/land breeze, we also adopted the same land-surface model. In addition, the simple explicit microphysical parameterisation for cloud water, rainwater, and ice (Dudhia 1993) and the Grell convective parameterisation scheme (Grell 1993) were used in our simulations. A cloud radiation scheme was used for shortwave radiation processes while a rapid radiative transfer model (Mlawer et al. 1997) was used for longwave radiation processes.

The three domains (D1, D2, and D3) in Seto-MM5 were initialised with the grid-point mesoscale model (MSM) re-analysis data, which were produced by the Japanese Meteorological Agency non-hydrostatic model (Saito et al. 2006). The MSM re-analysis data are available from 22.4°N to 47.6°N and 120°E to 150°E with a resolution of $0.1° \times 0.125°$ at 16 pressure levels and a time interval of 3 h (Saito et al. 2006). The lateral boundary conditions for D1 were also supplied by the MSM re-analysis data.

An accurate SST field is an important boundary condition for this study. We used the SST from the Marine Information Research Center (MIRC) in Japan for the domain inside the Seto Inland Sea. The initial MIRC SST is from monthly hydrographic survey data, and is available from 1964 to 1993. Figure 2 shows the SST distribution in the D3 domain in August, averaged over the period of 1964–1993. Two low SST areas are apparent near the Hayasui Strait and south of Aki-nada, respectively (see Fig. 1b for the names used in text: 'nada' is a Japanese word denoting a wide-water like bay). For the domain outside the Seto Inland Sea, we used the operational SST and sea-ice analysis data, which combine satellite data from the group for high resolution SST and in situ observations (Stark et al. 2007).

The simulation period was selected as 0000 UTC (0900 LST) 5th August to 0000 UTC (0900 LST) 7th August 2006 when the seasonal winds were weak and the weather conditions stable. The initial conditions for surface winds and surface pressure fields are given in Fig. 2c and d. The observation data used to validate model results were from the Automated Meteorological Data Acquisition System (AMeDAS), operated by the Japanese Meteorological Agency.

3 Results and Analysis

3.1 Comparison with Observations

Both the Seto-MM5 results and MSM re-analysis data were interpolated to all the AMeDAS observatories in the D3 domain (see Fig. 1b for their positions) and compared with observations to confirm the precision of the two models. Two statistical parameters, the root-mean-square-error (*RMSE*) and mean error (*MEAN*), were calculated from,

$$RMSE = \sqrt{\frac{\sum_{i=1}^{i=N} \left(X_m^i - X_a^i\right)^2}{N}}, \tag{1}$$

Table 1 Comparison of MSM and Seto-MM5 results with observations from 86 AMeDAS observatories in the D3 domain

	MSM	Seto-MM5
RMSE of wind speed ($m\,s^{-1}$)	1.23	1.32
MEAN of wind speed ($m\,s^{-1}$)	0.94	1.06
RMSE of temperature (K)	2.08	1.88
MEAN of temperature (K)	1.81	1.61

The wind speed is at the height of 10 m while the air temperature is at a height of 2 m. See text for definitions of *RMSE* and *MEAN*

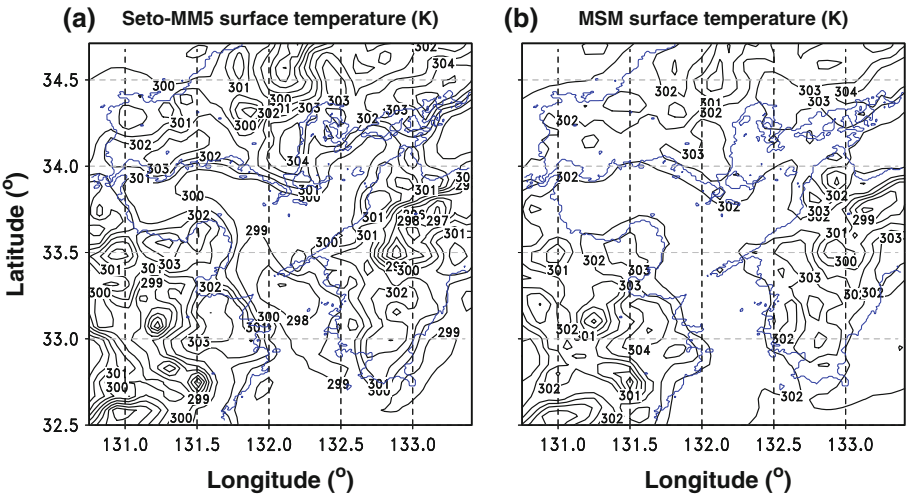

Fig. 3 Horizontal distributions of surface temperature at 2-m height simulated by the Seto-MM5 using MIRC SST (**a**) and that from MSM (**b**). Time of **(a)** and **(b)** was 1500 LST on 6 August 2006, 30 h after the Seto-MM5 simulation commenced

$$MEAN = \frac{1}{N}\sum_{i=1}^{i=N}\left|X_m^i - X_a^i\right|, \tag{2}$$

where X_m denotes the model variable, X_a is the corresponding variable for the AMeDAS observations, N is the data number, and i is the station number. We choose surface wind speed and surface air temperature as comparison variables. According to Table 1, the Seto-MM5 had the same precision as the MSM at the AMeDAS observatories.

Although the MSM and Seto-MM5 show little difference in the statistical parameters compared to observations over the land, they presented an apparent difference in the horizontal distribution of surface air temperature and winds over the sea. As an example, we present the surface air temperature over the sea from two models in Fig. 3. The surface air temperature in the Seto-MM5 responded well to the two lowest SST areas in the prescribed MIRC SST distribution (Fig. 2b) and showed a clear gradient of the surface air temperature over the sea (Fig. 3a), while for the MSM results the surface air temperature was generally uniform (Fig. 3b).

3.2 Harmonic Analysis on the Near-Surface Winds

According to the wind-fields at every hour (figures not shown here), the surface wind simulated by the Seto-MM5 was stronger over the sea than over the land. The MSM gave a more uniform and weaker wind field than Seto-MM5. An alteration of wind direction can be found in the results of Seto-MM5. The south-westerly landward flow in the daytime turned to a northerly or easterly seaward wind at night over Iyo-nada. This alteration could also be confirmed at the AMeDAS observatories along the coast but was not well represented by the MSM.

To separate the mean and diurnal variation components in the wind fields during the simulation period, we carried out a harmonic analysis, in which eastward and northward components of the wind are represented by following equations,

$$u(t) = \bar{u} + a_u \sin \omega t + b_u \cos \omega t + res_u \tag{3a}$$

$$v(t) = \bar{v} + a_v \sin \omega t + b_v \cos \omega t + res_v \tag{3b}$$

where, u and v denote the eastward and northward wind component, t is time, $\bar{u}$, $\bar{v}$ are the mean values, ω is the diurnal frequency, a_u, a_v, b_u and b_v are four harmonic constants for the diurnal variation with the unit of velocity; and res is the residual. Using the least squares method to minimize the residual res, the mean value ($\bar{u}$, $\bar{v}$) and four harmonic constants can be obtained from hourly model results or observations during the simulation period. The diurnal variation of the wind vector forms an ellipse whose major axis and orientation can be calculated from the four harmonic constants. The major axis denotes the magnitude of the diurnal wind variation while the orientation of the axis gives the direction of the strongest diurnal wind component: 48 h of AMeDAS data, Seto-MM5 and MSM results from 0100 UTC on 5 August to 0000 UTC on 7 August were used to calculate the mean values and harmonic constants in Eqs. 3a and 3b.

The daily mean winds at the observatories along the western Seto Inland Sea coast were generally weak except for the northern coastal location of Suo-nada (Fig. 4a, c). In general, the Seto-MM5 model overestimated the mean wind at several AMeDAS observatories (Fig. 4a) while the MSM underestimated the mean wind at most observatories (Fig. 4c). The strong westward mean wind along the northern coast of Suo-nada is reproduced by the Seto-MM5 but not found in the MSM results.

The major axes of the diurnal wind ellipses are perpendicular to the coastline at most observatories (Fig. 4b, d), a feature of the sea/land breeze. The lengths of the ellipse's major axes at the observatories indicate a large spatial variation in the magnitude of the diurnal wind variations. For example, the diurnal wind variations were apparent along the south coast of Suo-nada, but weak along the northern coast. The Seto-MM5 reproduced well the features of the diurnal wind variations (Fig. 4b) while the MSM apparently underestimated the magnitude of the diurnal wind variations (Fig. 4d).

Generally, the sea/land breeze over land weakens with distance from the coast; this feature is demonstrated by the magnitudes of the diurnal wind variations, which were calculated using both observations and model results (Seto-MM5 and MSM) at all the AMeDAS observatories in the D3 domain, versus the distance from the coast (Fig. 5). The observations for AMeDAS suggest that the penetration distance of the sea/land breeze to the land during the simulation period was approximately 20 km, within which the magnitude of the sea/land breeze fell sharply in the area over a distance less than 5 km from the coast. The Seto-MM5 model reproduced a strong diurnal variation of wind speed over the area close to the coast but overestimated the diurnal variation for the area greater than 5 km from the coast. The MSM failed to reproduce the strong diurnal variations of wind over the area close to the coast.

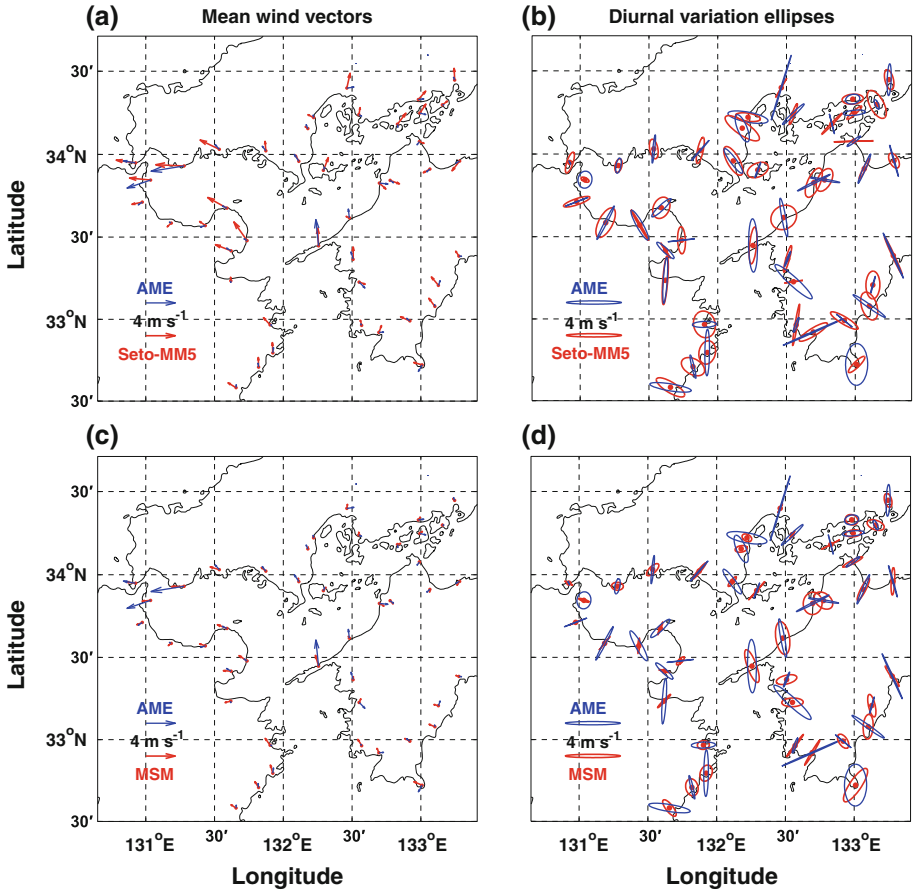

Fig. 4 Mean surface winds from a harmonic analysis from results of Seto-MM5 (*red arrows* in **a**), those of MSM (*red arrows* in **c**), and those of observations (*blue arrows* in **a** and **c**). Diurnal variations in surface winds from results of Seto-MM5 (*red ellipses* in **b**), those of MSM (*red ellipses* in **d**), and those of observations (*blue ellipses* in **b** and **d**). AMeDAS observatories in **a**–**d** are limited to those with a distance of less than 10 km from the coast

3.3 Sensitivity Experiments

In order to examine the influence of the SST and the SST gradient on the wind fields calculated by the Seto-MM5, two additional experiments were carried out. One used a uniform SST of 296 K (CSST case) and the other 300 K (WSST case). The two values of SST represent the lowest and highest SSTs in our study area. In two additional experiments, only the SST in the D3 domain was changed while the other model parameters, as well as the initial and boundary conditions, were the same as in the control simulation using realistic SST (MSST case). Since the change of the SST affects both the mean and diurnal components of the wind fields, we again used the harmonic analysis to separate them.

There was little change in the direction of the mean winds among the three cases, while the change was relatively apparent in the magnitude of the mean winds (Fig. 6a, c, e). A strong southerly or south-easterly wind can be found over the area from the Bungo Channel

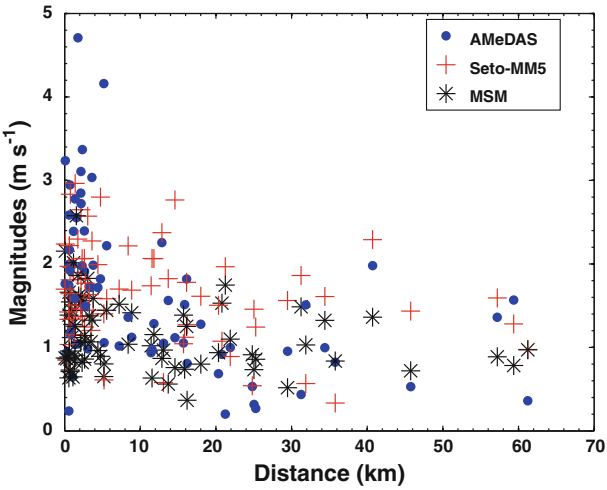

Fig. 5 Reduction in the diurnal variation magnitude in surface winds (*ordinate*) with distance from the coast (*abscissa*) as given at all AMeDAS observatories in the D3 domain for the results of Seto-MM5 (*red crosses*), those of MSM (*black stars*) and the observations (*blue dots*)

to Suo-nada. Its magnitude over the northern part of Bungo Channel and south-western part of Iyo-nada is larger in the WSST case (Fig. 6c) than in the other two cases. The low SST associated with the tidal front in the MSST case and the low SST itself in the CSST case weakened the winds over those areas. The south-easterly wind in Suo-nada is stronger in the MSST case than in the WSST and CSST cases, suggesting a possibility of acceleration in the MSST case as the air flows from cold to warm water. In the next section, we discuss this possibility by examining the change in the terms in the momentum equations with SST variations.

The magnitudes of diurnal components in the wind field from the MSST case (Fig. 6b) suggest that there are apparent diurnal variations with a magnitude larger than $2\,\mathrm{m\,s^{-1}}$ from the Bungo Channel towards Hiroshima Bay along the eastern part of Iyo-nada, whereas the mean wind is relatively weak. It is therefore expected that the wind changes direction from daytime to nighttime in these areas where the magnitude of the diurnal components are larger than the mean wind speed. The diurnal variation is generally weak over Suo-nada and can therefore affect only the wind speed there. It is worth noting that the apparent diurnal variation ($>2\,\mathrm{m\,s^{-1}}$) of wind speed occurs in a larger range (>10 km offshore) over the sea than over the land (<10 km from the coast, Fig. 5).

Compared with the CSST case (Fig. 6f), the WSST case expanded the area where the magnitudes of the diurnal component are larger than $2.5\,\mathrm{m\,s^{-1}}$. Such intensification is apparent over the Bungo Channel, the western part of Iyo-nada and Aki-nada (Fig. 6d). Differences in the diurnal variations between the MSST and CSST cases are not as apparent as the difference between the CSST and the WSST case. Therefore, the influence of SST itself on the diurnal wind variations is more important than that of the SST gradient due to the tidal front.

In summary, the Seto-MM5 reproduced well the spatial variation of mean winds and the diurnal wind variations in the Seto Inland Sea for a typical summer weather condition. Based on the Seto-MM5, the influence of SST variations due to a tidal front on the surface winds was examined with additional two sensitivity simulations, in which high and low uniform SST was specified, respectively. Comparison of two sensitivity simulations with the simulation

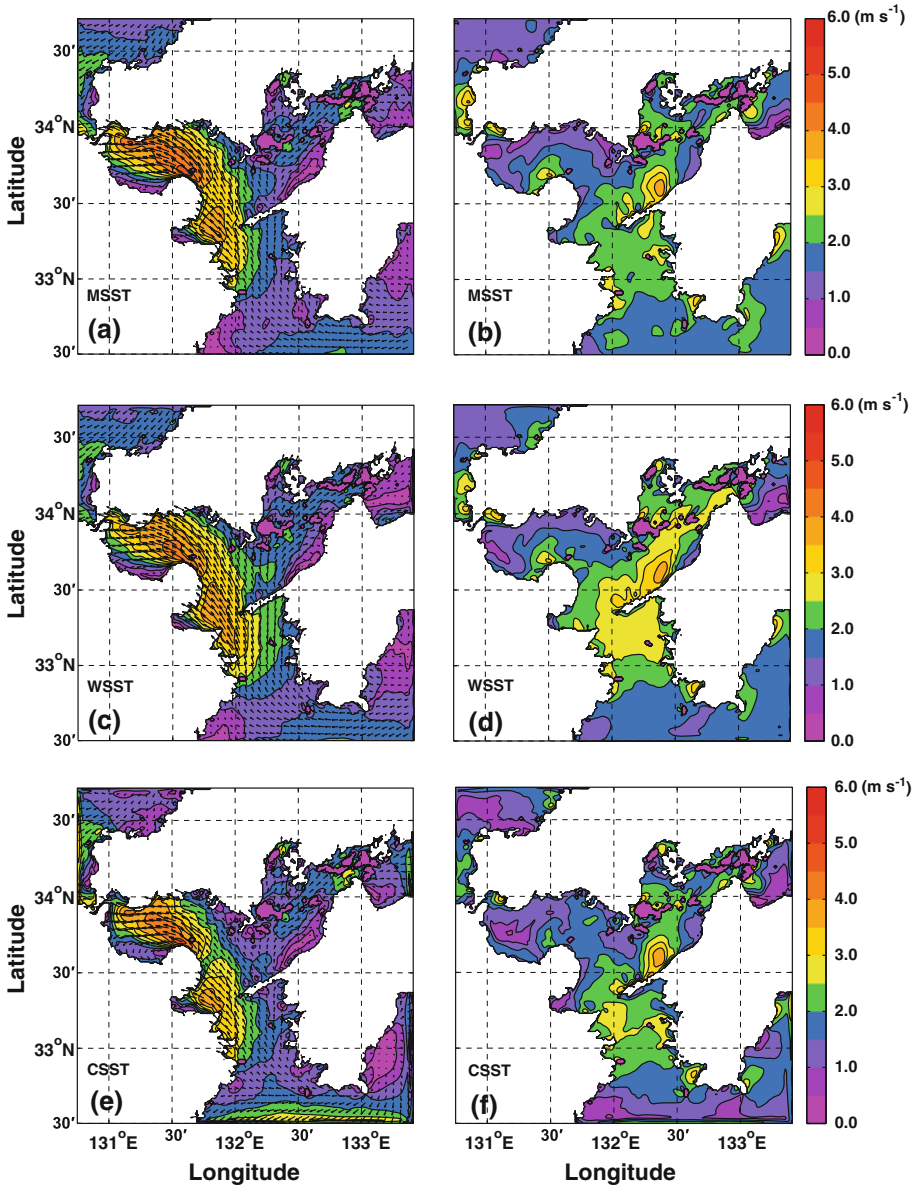

Fig. 6 Mean near-surface winds from the MSST case (**a**), from the WSST case (**c**) and from the CSST case (**e**); the magnitude of diurnal variation in near-surface winds from the MSST case (**b**), from the WSST case (**d**), and from the CSST case (**f**). *Shaded colours* in the *left panels* denote the mean wind speeds. The contour interval for all panels is $0.5\,\mathrm{m\,s^{-1}}$

using realistic SST indicated that the tidal front had significant influences on the mean winds over the sea. The presence of SST gradient around the tidal front had apparent influences on the mean surface wind speed. The mechanism responsible for the change in mean surface winds is further discussed below.

4 Dynamical Analysis and Discussions

The sensitivity analysis suggests an influence by both SST and SST gradients on the mean near-surface wind (Fig. 6a, c, e). To understand the physical processes that affect the response of the mean winds to the change in SST, we examined the terms in the momentum equations. Since the northward wind component is the major surface wind component across the tidal front, we focused on the northward wind component in the following discussion. The same procedures can be applied to the eastward wind component.

In terms of terrain-following σ coordinates (x, y, σ), the horizontal momentum equation of MM5 for the northward component (v) is:

$$\frac{\partial v(t)}{\partial t} = P + A + C + R + VD + HD, \tag{4}$$

where t is time, and P, A, C, R, VD and HD denote the terms of perturbation pressure gradient, advection, Coriolis force, curvature effect, vertical diffusivity and horizontal diffusivity, respectively. Detailed expressions for these terms are:

$$P = -\frac{m}{\rho}\left(\frac{\partial p'}{\partial y} - \frac{\sigma}{p^*}\frac{\partial p^*}{\partial y}\frac{\partial p'}{\partial \sigma}\right), \tag{5a}$$

$$A = -u\frac{\partial v}{\partial x} - v\frac{\partial v}{\partial y} - \dot{\sigma}\frac{\partial v}{\partial \sigma}, \tag{5b}$$

$$C = -fu + ew\sin\alpha, \tag{5c}$$

$$R = -u\left(u\frac{\partial m}{\partial y} - v\frac{\partial m}{\partial x}\right) - \frac{vw}{r_{earth}}, \tag{5d}$$

where m is a map-scale factor, ρ is density, p^* is the reference pressure defined as the pressure difference between the surface and top of atmosphere, p' is perturbation pressure; u, v and $\dot{\sigma}$ respectively denote eastward, northward and vertical velocity under the σ coordinates, $f = 2\Omega\sin\lambda$ and $e = 2\Omega\cos\lambda$, in which λ is latitude, Ω is the rate of the earth's rotation, $\alpha = \phi - \phi_c$, ϕ is longitude, and ϕ_c is the central longitude of the model domain; r_{earth} is the Earth's radius. Detailed expressions of VD and HD are not explained here but can be found in detail in Hong and Pan (1996).

4.1 Responses of Mean Wind and Forcing Terms to Variations in SST

The mean northward wind speed V during the simulation period (48 h) can be expressed as,

$$V = \frac{1}{n}\sum_{m=1}^{m=n} v_m = \frac{1}{n}\sum_{m=1}^{m=n}\left(v_0 + \Delta t\sum_{i=1}^{i=m} F_i\right) = v_0 + \frac{\Delta t}{n}\sum_{i=1}^{i=n}(n-i+1)\,F_i m, \tag{6}$$

where m is the index of the integration step, n is the number of total integration steps during the simulation period, v_m is the northward component of winds at an integration step m, Δt is the timestep, v_0 is the initial value, F is the sum of the right-hand side terms in Eq. 4 at each timestep. The difference in the mean wind speed from its initial value is expressed as,

$$V - v_0 = \frac{\Delta t}{n}\sum_{i=1}^{i=n}(n-i+1)\,F_i = SF. \tag{7}$$

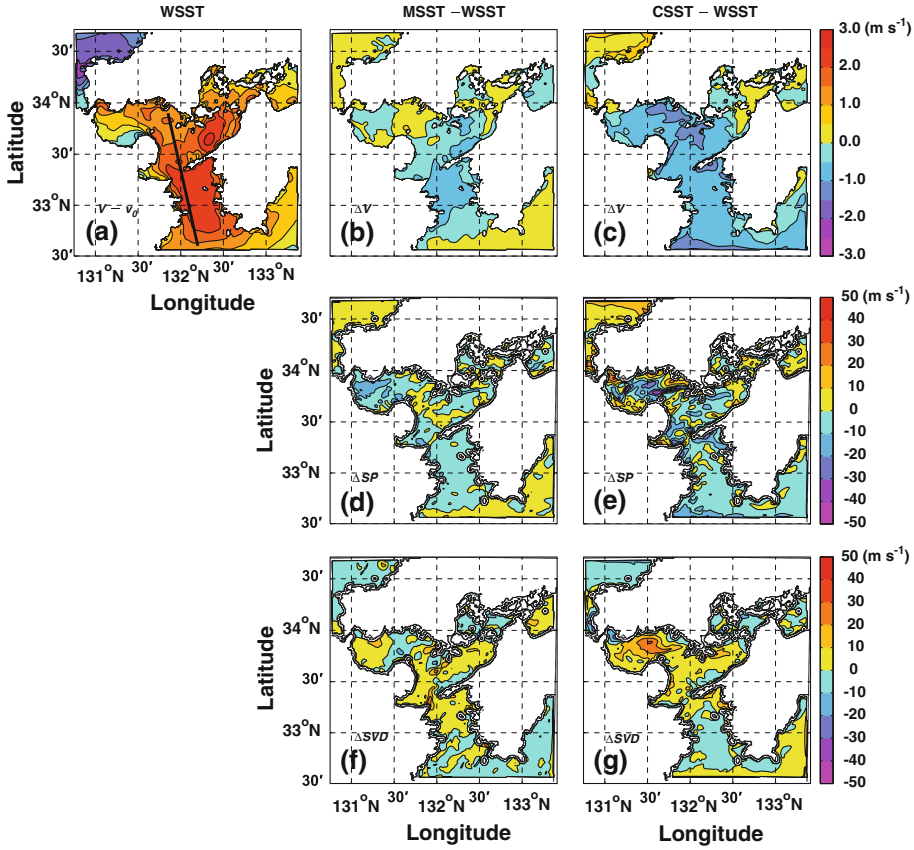

Fig. 7 Differences of the mean northward wind speed from the initial values in the WSST case (**a**). Difference in the mean northward wind speed ΔV, of the perturbation pressure gradient term ΔSP, and of the vertical diffusivity term ΔSVD between the MSST case and the WSST case (**b**, **d**, **f**), and between the CSST case and the WSST case (**c**, **e**, **g**). The wind curls near the coast (within two grids, 6 km from coast), where the variation was significantly influenced by the land, are not shown in **d**, **f**. The forcing terms in each case were calculated by the right-hand side of Eq. 7. Units are in $\mathrm{m\,s^{-1}}$ in all panels. *Black line* in **a** denotes a cross-section along which the vertical structure of potential temperature, perturbation pressure and northward wind speed are given in Figs. 10, 11, 12 and 14

According to Eq. 7, the difference of the mean northward wind speed from its initial value arises from SF, in which S is the arithmetic calculation in Eq. 7 whereas F is replaced by the right-hand side terms in Eq. 4. Consequently, SF includes the contribution from the terms of the perturbation pressure gradient (SP), advection (SA), Coriolis force (SC), curvature effect (SR), vertical diffusivity term (SVD) and horizontal diffusivity (SHD). During the simulations, each of the right-hand side terms in Eq. 4 was saved at every timestep and the arithmetic calculations in Eq. 7 were then carried out. From the examination of each term in SF, we determined which term was important in the wind development from the initial value. Furthermore, since the initial values v_0 were the same in the three cases of WSST, CSST and MSST, the difference in the mean northward wind component could be directly related to the response of the forcing terms in SF.

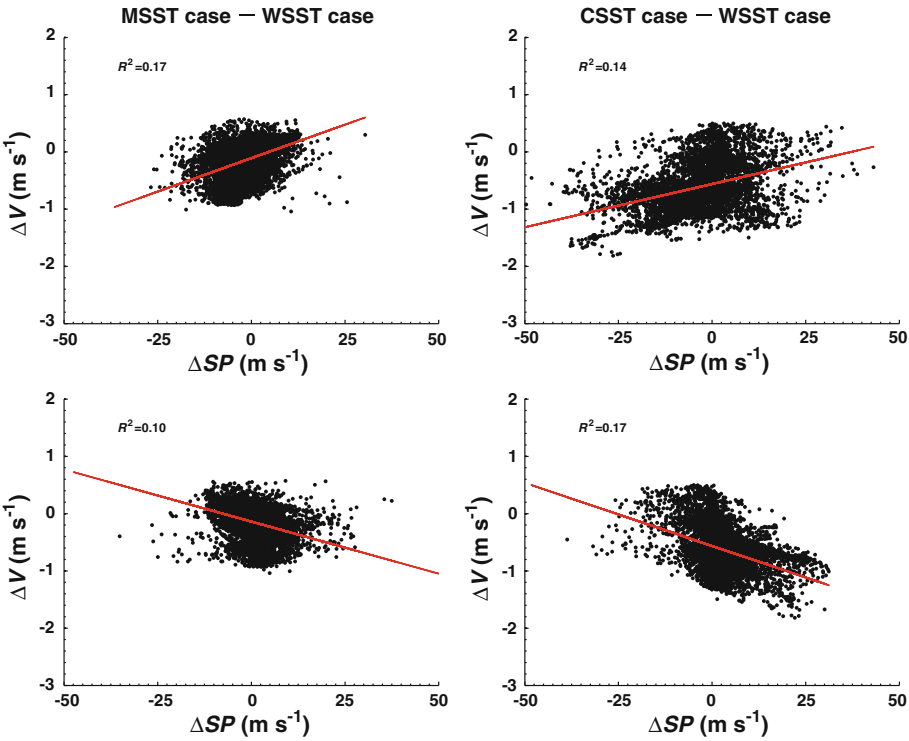

Fig. 8 The scatter plot of the difference in the mean northward wind speed ΔV versus the difference in the perturbation pressure gradient term ΔSP; and versus the difference in the vertical diffusivity term ΔSVD between the MSST case and the WSST case (**a**, **c**); and between the CSST case and the WSST case (**b**, **d**) at all sea grids in the D3 domain. The values less than $10^{-2}\,\mathrm{m\,s^{-1}}$ and the values at the closest three grids from coast were removed. The *red line* in each panel is the linear regression line given by the least-square method. R^2 is the determination coefficient

The differences of the mean northward wind components from the initial values in the WSST case (the difference between Figs. 6c and 2c) are the development of the northward wind speed over the entire domain (Fig. 7a). The mean northward wind speed is weaker in the MSST case than in the WSST case (Fig. 7b). Such a reduction in the mean northward wind speed is attributed mostly to the negative difference in the perturbation pressure gradient term between the two cases (Fig. 7d). The CSST case also simulated a weaker mean northward wind speed than did the WSST case (Fig. 7c). Such a change in wind speed is partly caused by the negative difference in the perturbation pressure gradient term (Fig. 7e) and partly from the negative difference in the vertical diffusivity term at the Bungo Channel (Fig. 7g). Since the advection and Colioris forces are directly affected by the wind speed variation rather than by variation of the underlying SST, and the curvature effect and horizontal diffusion were much smaller than the other terms, these forcing terms will not be discussed in detail.

Although both the perturbation pressure gradient term and vertical diffusivity term likely contribute to the variation in surface wind speed (Fig. 7), their effects were different (Fig. 8). The difference in the mean northward wind speed (ΔV) between the MSST case and the WSST case has an apparent positive linear relationship with the difference in the perturbation pressure gradient term (ΔSP) (Fig. 8a), and has a negative linear relationship with the

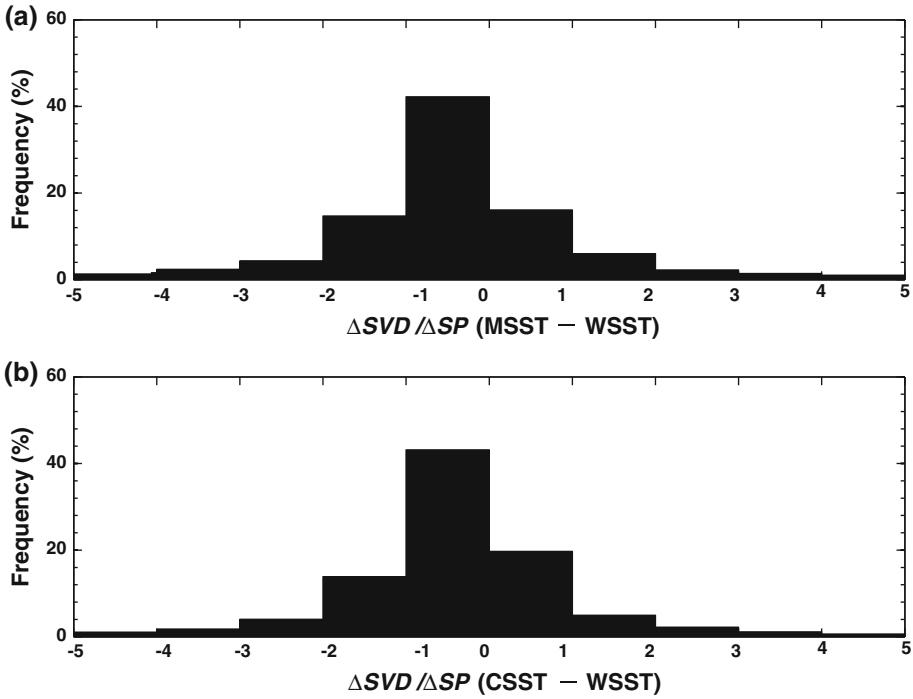

Fig. 9 Histogram of the occurrence frequency for the ratio of the difference in vertical diffusivity term ΔSVD to the difference in the perturbation pressure gradient term ΔSP between the MSST case and the WSST case (**a**); between the CSST case and the WSST case (**b**). The ratio was calculated from the values given in Fig. 8. The *abscissa* denotes the range of ratio and the *ordinate* denotes the occurrence frequency. There are ten ranges for the ratio from −5 to 5 with an interval of one as shown in the *abscissa*

difference in the vertical diffusivity term (ΔSVD) (Fig. 8c). The same positive and negative linear relationships can also be confirmed between the CSST case and the WSST case (Fig. 8b, d). The Fisher–Snedecor F-test was used to further examine the significance of the linear regressions in Fig. 8. For the significance level $\alpha = 0.01$, the critical value of the determination coefficient is 4.6×10^{-4} for the sample number ($n = 14277$) in Fig. 8. Therefore, the linear regressions in Fig. 8 were significant because the determination coefficients in Fig. 8 were much larger than the critical value.

Two new variables were defined to further examine the relative importance of perturbation pressure gradient and vertical diffusivity terms. The ratio of the perturbation pressure gradient term to the vertical diffusivity term was defined as $\eta = \Delta SVD/\Delta SP$. The occurrence frequency of the ratio was defined as $f(\eta) = \gamma/\zeta$, where ζ is the total number of sea-grid points at which η was calculated; γ is the number of grid points where η is within a given range. The occurrence frequencies of the ratio from −5 to 5, with an interval of 1, are presented in Fig. 9. Beyond the range from −5 to 5, the occurrence frequency is small enough to be neglected.

The occurrence frequency in the range $-1 < \eta < 0$ was over 40% (Fig. 9), suggesting that for over 40% of the total sea surface, the difference in vertical diffusivity has an opposite sign to, but smaller magnitudes than, the difference in the perturbation pressure gradient. The occurrence frequency in the range $|\eta| < 1$ was larger than 60% (Fig. 9a, b), indicating

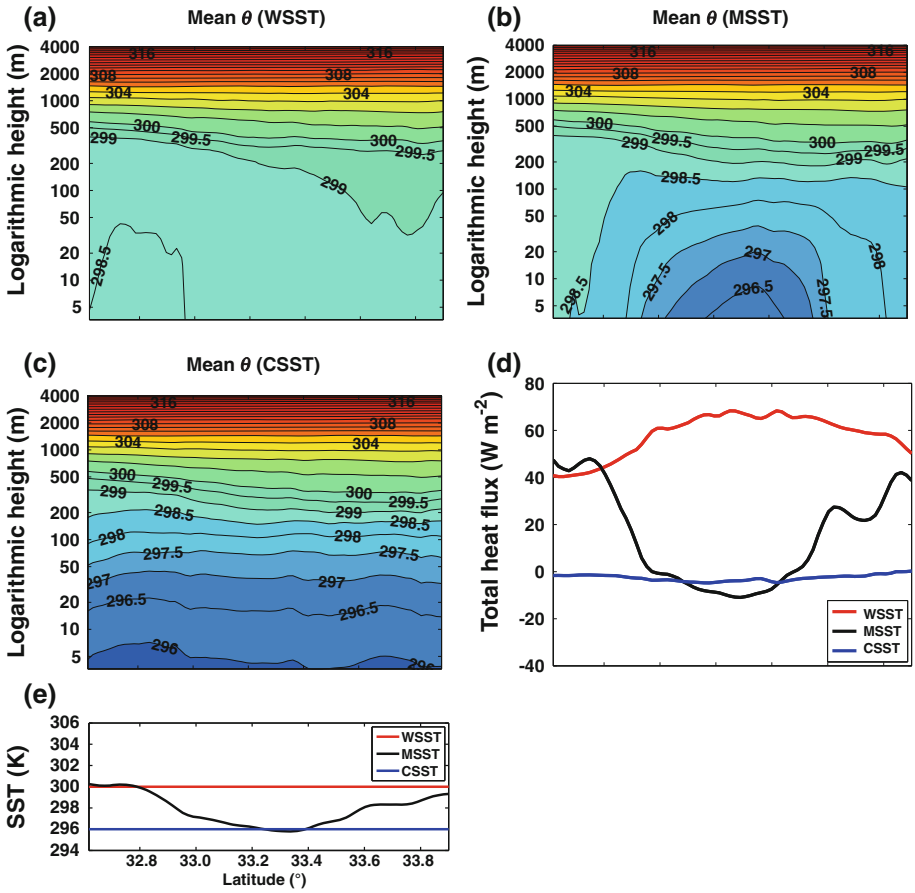

Fig. 10 Vertical distribution of the mean potential temperature (K) simulated by the WSST case (**a**), by the CSST case (**b**), and by the MSST case (**c**) at the cross-section shown in Fig. 7a. The *abscissa* denotes latitude and the *ordinate* denotes the logarithm of height. The sum of the sensible and latent total fluxes (**d**) and the SST distribution (**e**) along the cross-section are shown in three cases

the area, for which the difference in vertical diffusivity is generally smaller than that in the perturbation pressure gradient, is over 60% of the total sea surface.

Therefore, the perturbation pressure gradient is more effective than diffusivity in modifying the sea-surface wind.

4.2 Response of Vertical Structure to Variations in SST

To understand the extent to which the SST affects the vertical structure of the marine atmospheric boundary layer, we examined the vertical distributions of several variables along a section across the tidal front (Fig. 7a).

According to the vertical distribution of the potential air temperature along a cross-section, the air is well mixed in the WSST case (Fig. 10a) and the mixed layer reaches a height of over 200 m. In the MSST case, the mixed layer is over 200 m in depth in the southern high SST area, nearly disappears over the central low SST area, and then redevelops in the northern

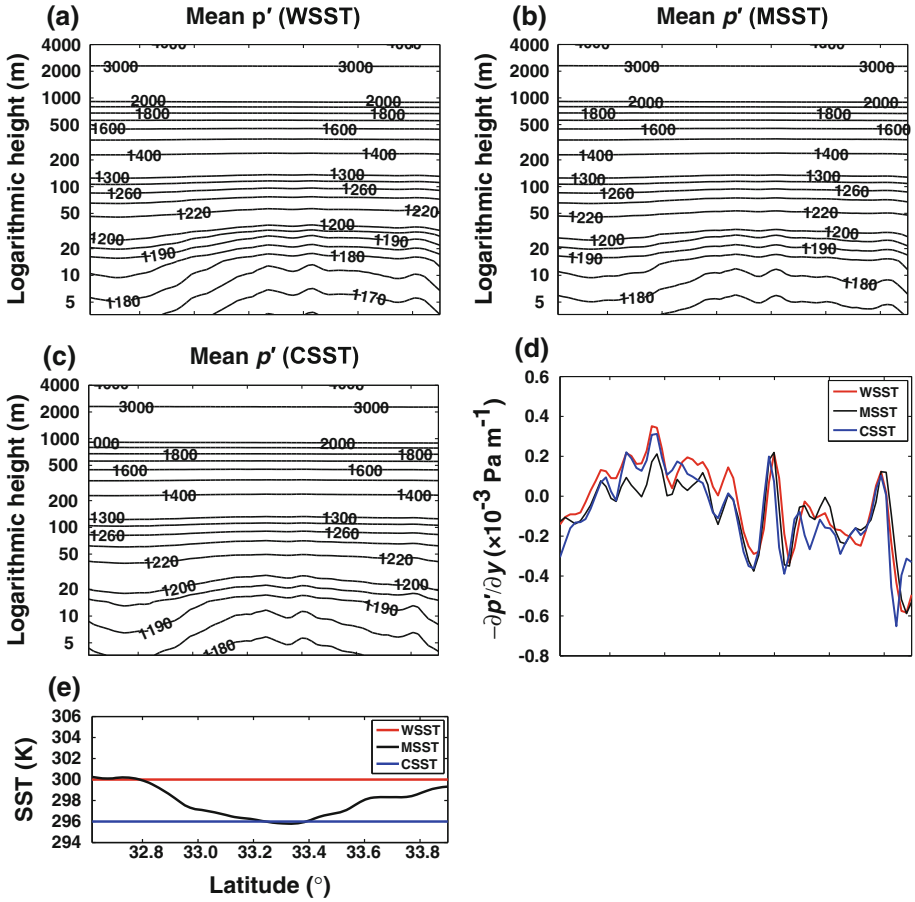

Fig. 11 Same as Fig. 10 but for the mean perturbation pressure (Pa) in three cases (**a**–**c**) and the meridional gradient of perturbation pressure in three cases along the cross-section (**d**)

high SST area (Fig. 10b). The mixed layer nearly disappears in the CSST case, giving an apparent stable stratification along the cross section (Fig. 10c).

The air inside the mixed layer was heated by warm sea water with high SST in the WSST case. The surface potential temperature in the WSST case (≈298.5 K) was lower than the underlying SST (≈300 K), but that in the CSST case (≈295.5 K) was close to the underlying SST (≈296 K). The positive air-sea temperature difference in the WSST case produced the largest total flux (the sum of the latent and sensible heat fluxes) from the sea to the air (red line in Fig. 10d) in three cases, which increased the mixed-layer height. The small air-sea temperature difference in the CSST case reduced the total flux from the sea to the air almost to zero (blue line in Fig. 10d), and maintained stratification in the air. The MSST case released nearly the same total flux over the two sides of the cross-section as did the WSST case, but a small or even negative total flux in the central area of the cross-section occurred (black line in Fig. 10d), therefore limiting the development of a mixed layer in that area.

In all three cases, the surface mean perturbation pressure was low in the central area and high on the two sides of the cross-section (Fig. 11a–c). As a result, the northward pressure gradient forcing (Fig. 11d) accelerates the northward wind component from the southern

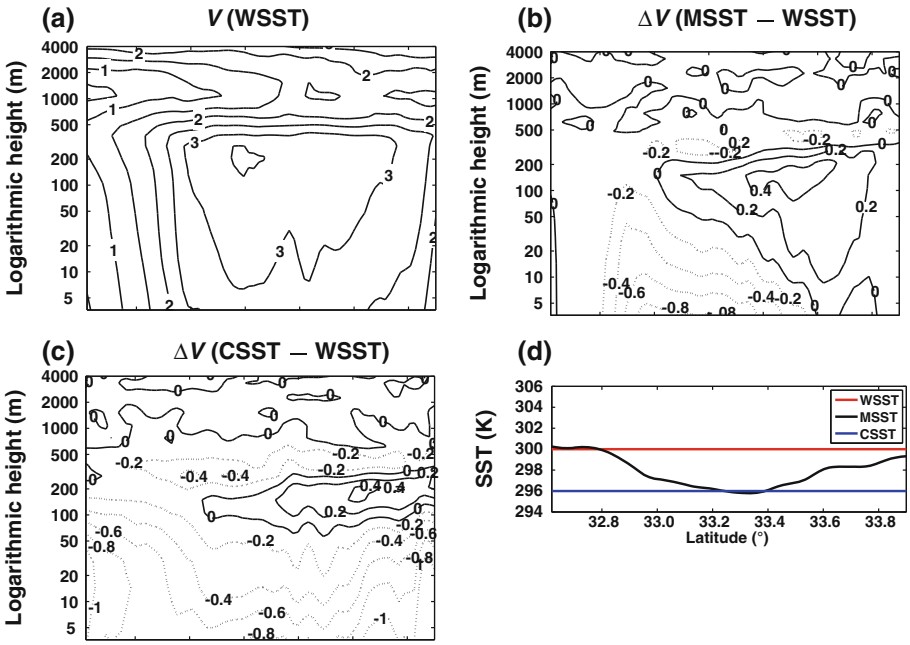

Fig. 12 Same as Fig. 10 but for the mean northward wind speed ($m\,s^{-1}$) of WSST case (**a**), the difference in the mean northward wind speed between the MSST case and the WSST case (**b**), and that between the CSST case and the WSST case (**c**). The *dashed contour lines* in **b** and **c** show the reduction of the northward wind speed

side to the central area of the cross-section, while the southward pressure gradient forcing decelerates the northward wind component from the central area to the northern side of the cross-section (Fig. 12a). The change in air density with potential temperature affected the surface perturbation pressure distribution and therefore modified the surface winds.

The potential air temperature over the central area of the cross-section was lower in the MSST case than in the WSST case. As a result, the denser air due to a lower potential temperature increased the surface perturbation pressure at the central area and consequently changed the horizontal perturbation pressure gradient. In the southern section, where the air flows from the high SST area to the low SST area, the surface perturbation pressure in the MSST case was nearly the same as that in the WSST case over the high SST area, but it increased over the low SST area (Fig. 11b). Such variations in the MSST case weakened the northward pressure gradient forcing (Fig. 11d, 32.8°N–33.3°N), as well as an increase of the northward surface wind speed, which resulted in a lower northward surface wind speed over the southern tidal front than in the WSST case (Fig. 12b). In the northern area where the air flows from low to high SST area, the increase in SST from the central to the northern area weakens the southward pressure gradient forcing (Fig. 11d, 33.5°N–33.8°N) as well as a decrease of the surface northward wind speed. Therefore, the surface northward wind speed is a little larger in the MSST case than in the WSST case (Fig. 12b).

A similar explanation can also be applied to the CSST case. Denser air in the CSST case increased the surface perturbation pressure through the cross-section, and changed the horizontal gradient of the surface perturbation pressure. In the southern area of the cross-section,

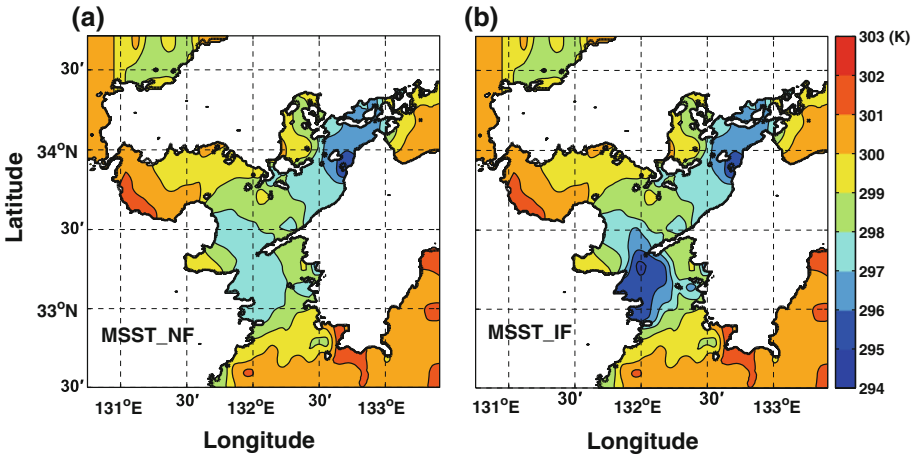

Fig. 13 Horizontal distribution of SST in the case without the tidal front (**a**, MSST_NF), and in the case with an intensified tidal front (**b**, MSST_IF) at the Haysui Strait. In the case of MSST_NF, SST less than 298 K around the Hayashui Strait was set to 298 K. In the case of MSST_IF, the original in situ SST inside the Hayashui Strait was reduced by 1 K and re-interpolated

the northward pressure gradient forcing was weaker in the CSST case than in the WSST case (Fig. 11d, 32.8°N–33.3°N). Consequently, the acceleration of the northward wind from the southern to the central area was weaker in the CSST case than in the WSST case. At the northern side of the cross-section, the southward pressure gradient forcing was stronger in the CSST case than in the WSST case (Fig. 11d, 33.5°N–33.8°N) and therefore deceleration was stronger in the CSST case than in the WSST case. As a whole, the surface northward wind component was weaker in the CSST case than in the WSST case (Fig. 12c).

In addition to the change in pressure gradients with SST, the vertical profile of the wind speed also corresponded to the development of the mixed layer, which was strongly affected by the underlying SST. The maximum northward wind speed occurred at a height of approximately 200 m. Below this, the WSST case produced a well-mixed wind-speed profile at the cross-section (Fig. 12a) while the CSST case produced strong shear as implied by the differential reduction in wind speed in the vertical direction (Fig. 12c). In the MSST case (Fig. 12b), the wind speed profile was well-mixed over the high SST area but sheared over the low SST area.

The variations in SST (Fig. 2b) include two parts: the first is for a slow change from the offshore to the inland sea, and the second is the abrupt change near the Hayasui Strait due to the presence of the tidal front. Since the SST used in the MSST case is an average of data from 1964 to 1993, it may weaken the intensity of the tidal front. In order to examine the influence of tidal front intensity on the near-surface winds, we carried out two additional simulations in which only the abrupt SST change near the tidal front was artificially modified. One simulation used the MSST without the tidal front at the Hayasui Strait (Fig. 13a, MSST_NF in short), the other used the MSST with an enhanced tidal front at the strait (Fig. 13b, MSST_IF in short). The two additional simulations confirmed that the presence of the tidal front weakens the winds in the area upwind of the front and intensifies the winds downwind of the front (Fig. 14b). Moreover, this effect is likely in proportion to the intensity of the tidal front (Fig. 14b, c).

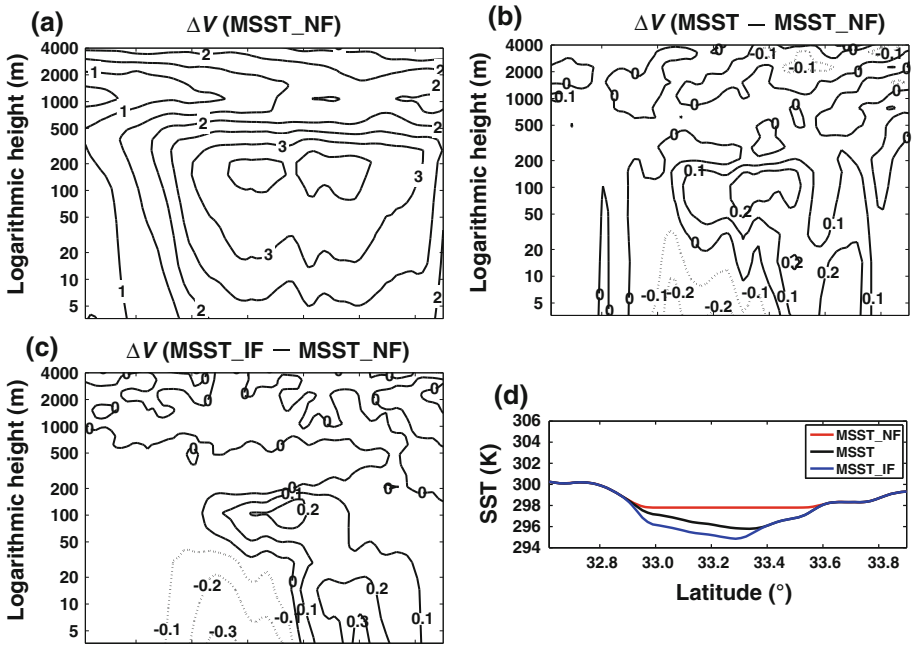

Fig. 14 Vertical distribution of mean northward wind speed ($m\,s^{-1}$) simulated by the MSST_NF case (**a**) and the differences in mean northward wind speed between the MSST case and the MSST_NF case (**b**) and that between the MSST_IF case and the MSST_NF case (**c**) at the cross-section shown in Fig. 7a. The *abscissa* in panels (**a**–**c**) denotes latitude and the *ordinate* denotes the logarithm of height. The *dashed contour lines* in **b** and **c** show the reduction of the northward wind speed. The distribution of SST along the cross-section in the MSST_NF case (*red line*), the MSST case (*black line*) and the MSST_IF case (*blue line*) is shown in **d**

5 Summary

A regional numerical model of the atmosphere, referred to as Seto-MM5, was configured for an inland sea in Japan to examine the influence of variations in SST associated with a tidal front on the surface winds. The Seto-MM5 reproduced well the spatial variation in mean winds, and captured the essential features of diurnal variation in winds, i.e., sea/land breeze, which were also confirmed in observations.

Comparison of two sensitivity simulations, which used spatially uniform high and low SSTs, along with the control simulation using realistic SST, indicated that the mean winds over the sea were affected by both the SST magnitude and its horizontal gradient, while variations in diurnal winds over the sea were affected more by the SST magnitude than by its gradient. Among the results from the three simulations, the direction of the mean winds showed little difference but the magnitude of the mean winds showed apparent differences. The simulation with high (low) SST gives strongest (weakest) mean winds over most areas. The simulation with realistic SST gave a weak mean wind over the area upwind of the tidal front and a strong mean wind downwind of the front, suggesting that the presence of the tidal front likely decelerates the mean winds in the upwind area and accelerates the mean winds in the downwind area.

The changes in the terms of the momentum equations with variations in SST show that the variation in the perturbation pressure gradient is the dominant factor determining the response

of surface winds to variations in SST. The vertical diffusivity operates as the secondary factor in changing the surface wind. Variations of other terms in the momentum equations depended closely on the modification of the surface winds but not on the SST and therefore were not discussed in detail.

The perturbation pressure was thermally related to the underlying SST. When the air flows from a high SST area to a low SST area, i.e., entering a tidal front, the air progressively becomes cooler and its density increases. The denser air increases the surface perturbation pressure, which induces an additional pressure gradient force with a direction from the low SST area to the high SST area, and therefore weakens the surface wind speed upwind of the front. On the other hand, when the air flows from a low SST area to a high SST area, i.e., departing a tidal front, the situation is reversed and the surface wind downwind of the front is intensified.

Although the spatial scale of SST fronts in this study are much smaller than that used by Song et al. (2006), our results are consistent with their conclusion that the perturbation pressure gradient is the dominant force modifying surface winds over a SST front. In this sense, our study expands on their results to the relationship between summer coastal winds and tidal fronts. However, because of the small scale of the tidal front, the deceleration and acceleration of the surface winds in the areas upwind and downwind of the front are weaker than those occurring over fronts in the open ocean.

Acknowledgments The mesoscale model re-analysis data used in this study were obtained from the data server of the Research Institute for Sustainable Humanosphere, Kyoto University. We thank Drs. Gao HW, Zhao L, Gao SH and Wang Q for their useful suggestions and comments. This study was supported by the Global COE (Centers of Excellence) Program and the Grants-in-Aid for Scientific Research (22106002) from the Ministry of Education, Culture, Sports, Science and Technology, Japan. We thank reviewers for their insightful and constructive comments.

References

Chelton DB, Esbensen SK, Schlax MG, Thum N, Freilich MH, Wentz FJ, Gentemann CL, McPhaden MJ, Schopf PS (2001) Observations of coupling between surface wind stress and sea surface temperature in the Eastern Tropical Pacific. J Clim 14(7):1479–1498

Chelton DB, Schlax MG, Freilich MH, Milliff RF (2004) Satellite measurements reveal persistent small-scale features in ocean winds. Science 303:978–983

Chelton DB (2005) The impact of SST specification on ECMWF surface wind stress fields in the Eastern Tropical Pacific. J Clim 18(4):530–550

Chen CS, Beardsley RC, Hu S, Xu Q, Lin HC (2005) Using MM5 to hindcast the ocean surface forcing fields over the Gulf of Marine and Georges Bank region. J Atmos Ocean Technol 22(2):131–145

Chen F, Dudhia J (2001) Coupling and advanced land surface-hydrology model with the Penn State–NCAR MM5 modelling system, Part I: model implementation and sensitivity. Mon Weather Rev 129(4):569–585

Dudhia J (1993) A nonhydrostatic version of the Penn State–NCAR mesoscale model: validation tests and simulation of an Atlantic cyclone and cold front. Mon Weather Rev 121(5):1493–1513

Grell GA (1993) Prognostic evaluation of assumptions used by cumulus parametreisations. Mon Weather Rev 121(3):764–787

Grell GA, Dudhia J, Stauffer DR (1994) A description of the fifth-generation Penn State/NCAR mesoscale model (MM5). NCAR Tech Note, NCAR/TN-398+STR, 122 pp. http://nldr.library.ucar.edu/collections/technotes/asset-000-000-000-214.pdf

Hayes SP, McPhaden MJ, Wallace JM (1989) The influence of sea surface temperature on surface wind in the eastern equatorial Pacific: weekly to monthly variability. J Clim 2(12):1500–1506

Hong SY, Pan HL (1996) Non-local boundary layer vertical diffusion in a medium range forecast model. Mon Weather Rev 124(10):2322–2339

Lindzen R, Nigam S (1987) On the role of sea surface temperature gradients in forcing low-level winds and convergence in the tropics. J Atmos Sci 44(17):2418–2436

Lo JCF, Lau AKH, Chen FJ, Fung CH, Leung KKM (2007) Urban modification in a mesoscale model and the effects on the local circulation in the Pearl River Delta region. J Appl Meteorol Climatol 46(4):457–476

Mahrt L, Vickers D, Moore E (2004) Flow adjustments across sea-surface temperature changes. Boundary-Layer Meteorol 111(3):553–564

Minobe S, Kuwano-Yoshida A, Komori N, Xie SP, Small RJ (2008) Influence of the Gulf Stream on the troposphere. Nature 452:206–209

Mizuma M (1995) General aspects of land and sea breezes in Osaka Bay and surrounding area. J Meteorol Soc Jpn 73(6):1029–1040

Mizuma M (1998) General aspects of land and sea breezes in western Seto Inland Sea and surrounding areas. J Meteorol Soc Jpn 76(3):403–418

Mlawer EJ, Taubman SJ, Brown PD, Iacono MJ, Clough SA (1997) Radiative transfer for inhomogeneous atmosphere: RRTM, a validated correlated-k model for the longwave. J Geophys Res 102(D14):16663–16682

Nonaka M, Xie SP (2003) Covariations of sea surface temperature and wind over the Kuroshio and its extension: evidence for ocean-to-atmosphere feedback. J Clim 16(9):1404–1413

Saito K, Fujita T, Yamada Y, Ishida JI, Kumagai Y, Aranami K, Ohmori S, Nagasawa R, Kumagai S, Muroi C, Kato T, Eito H, Yamazaki Y (2006) The operational JMA nonhydrostatic mesoscale model. Mon Weather Rev 134(4):1266–1298

Simpson JE (1994) Sea breeze and local wind. Cambridge University Press, New York, 234 pp

Simpson JH, Hunter JR (1974) Fronts in the Irish Sea. Nature 250:404–406

Skyllingstad E, Vickers D, Mahrt L (2007) Effects of mesoscale sea-surface temperature fronts on the marine atmospheric boundary layer. Boundary-Layer Meteorol 123(2):219–317

Small RJ, DeSzoeke SP, Xie SP, O'Neill L, Seo H, Song Q, Cornillon P, Spall M, Minobe S (2008) Air-sea interaction over ocean fronts and eddies. Dyn Atmos Ocean 45(3–4):274–319

Song Q, Hara T, Cornillon P, Friehe CA (2004) A comparison between observations and MM5 simulations of the marine atmospheric boundary layer across a temperature front. J Atmos Ocean Technol 21(2):170–178

Song Q, Cornillon P, Hara T (2006) Surface wind response to oceanic fronts. J Geophys Res 111(C12):C12006

Stark JD, Donlon CJ, Martin MJ, McCulloch ME (2007) OSTIA: an operational, high resolution, real time, global sea surface temperature analysis system. In Proceedings of the Oceans 2007. Marine challenges: coastline to deep sea, Aberdeen, Scotland, IEEE/OES, 4 pp. http://ghrsst-pp.metoffice.com/pages/latest_analysis/docs/Stark_et_al_OSTIA_description_Oceans07.pdf

Takeoka H (2002) Progress in Seto Inland Sea research. J Oceanogr 58(1):93–107

Troen I, Mahrt L (1986) A simple model of the atmospheric boundary layer: sensitivity to surface evaporation. Boundary-Layer Meteorol 37(1–2):129–148

Wallace JM, Mitchell TP, Deser C (1989) The influence of sea surface temperature on surface wind in the eastern equatorial Pacific: seasonal and interannual variability. J Clim 2(12):1492–1499

Xie SP (2004) Satellite observations of cool ocean-atmosphere interaction. Bull Am Meteorol Soc 85(2):195–208

Yanagi T, Koike T (1987) Seasonal variation in thermohaline and tidal fronts, Seto Inland Sea, Japan. Cont Shelf Res 7(2):149–160

Yanagi T, Okada S (1993) Tidal fronts in the Seto Inland Sea. Mem Fac Eng Ehime Univ 12:61–67 (in Japanese)